Optimal Duty Ratio Assisted PFM Control for VHF Isolated Class E DC-DC Converter

Desheng Zhang, Liangliang Lu, Wei Song, Run Min, *Member, IEEE*, Qiaoling Tong, *Member, IEEE*, Qiao Zhang, *Member, IEEE*, Han Peng, *Senior Member, IEEE*, and Keliang Zhou, *Senior Member, IEEE*

***Abstract*—This article presents an optimal duty ratio assisted pulse frequency modulation control for very high frequency isolated class E dc–dc converter to achieve both continuous power flow and optimal switch timing. The continuous power flow significantly reduces output ripple of the converter, while the optimal switch timing guarantees consistent zero-voltage-switching (ZVS) and minimized reverse conduction loss. To pave the way for the proposed control, a resonant fitting model is established for deriving the optimal duty ratio and output power under dynamic switching frequency. The optimal duty ratio is calculated according to zero-crossing points of the switching node voltage (v_{ds}), and it aims to turn ON the power switch once v_{ds} reaches zero. This ensures consistent ZVS while preventing reverse conduction of gallium nitride (GaN) high electron mobility transistor (HEMT) when the switching frequency changes. Furthermore, the proposed control is integrated with ON/OFF modulation to extend load range of the converter. A 10–18 MHz prototype is built to verify effectiveness of the proposed control. Compared with conventional PFM control, the proposed control reduces the power loss by 35.9% at 40% load while maintains continuous power flow.**

***Index Terms*—Isolated class E dc–dc converter, optimal duty ratio, pulse frequency modulation (PFM), resonant fitting model, zero-voltage-switching (ZVS).**

I. Introduction

VERY high frequency (VHF) power converters feature a switching frequency above ten megahertz, which have been promoted by the rapid development of wide bandgap semiconductor devices [1], [2]. They are widely used in wireless power transfer, power amplifiers, and compact power supply applications, since high frequency can greatly reduce the energy buffer in power conversion [3], [4]. To promote the switching frequency above 10 MHz, soft-switching techniques are typically required, such as zero-voltage-switching (ZVS) and zero-current-switching (ZCS) [5], [6]. However, realization of soft-switching for VHF power converters highly depends on the operation conditions. When the operation condition deviates from the optimal point, ZVS failure may occur and harms the efficiency [7].

ON/OFF control has the advantages of consistent ZVS, fast dynamic response, high light load efficiency and simple realization [8], [9], which has been the most popular method for output voltage regulation of VHF power converters. Consistent ZVS can be achieved over a wide load range, as long as the ON-state is well tuned [10], [11], [12]. However, the intermittent power flow under ON/OFF control induces large low frequency ripple in output voltage and causes large mode transition losses. To address this issue, variable frequency (VF) ON/OFF and multipower level (MPL) ON/OFF are proposed to reduce the intermittent magnitude of power level [13], [14]. Furthermore, aiming at eliminating mode transient time, zero-transient ON/OFF control is proposed. With two extra power switch and two extra capacitors, the ON/OFF modulation frequency can be greatly increased to reduce the mode transition loss and ripple [15]. However, all above ON/OFF approaches cannot fully address the ripple and loss caused by mode transition.

Compared with ON/OFF approaches, cycling-skipping controls regulate the output voltage by skipping part of cycles in the rectifier stage, while maintaining continuous power flow in the inverter stage [16], [17], [18]. These methods achieve smaller filter and lower EMI than ON/OFF control, although the skipped cycles would cause much higher voltage stress on the rectifier diode. Out-phasing control regulates the output voltage by adjusting phase shift between two inverters [19], [20], [21]. This can ensure ZVS over the whole load range, but it suffers from degraded light-load efficiency and complex implementation.

In addition to above control methods, PFM can also continuously operate the converter, which reduces the low frequency output voltage ripple [22], [23]. However, when the switching frequency deviates from the optimal value, ZVS failure and reverse conduction loss will severely degrade the power efficiency. As shown in Fig. 1, when the switching frequency deviates above the optimal value, ZVS may fail that induces

Manuscript received 27 March 2023; revised 1 July 2023 and 16 August 2023; accepted 18 September 2023. Date of publication 22 September 2023; date of current version 23 October 2023. This work was supported by the National Natural Science Foundation of China under Grants 62074067 and 62374067. Recommended for publication by Associate Editor X. Ruan. *(Corresponding author: Run Min.)*

Desheng Zhang, Qiao Zhang, and Keliang Zhou are with the School of Automation, Wuhan University of Technology, Wuhan 430070, China (e-mail: dszhang@hust.edu.cn; zhangqiao@whut.edu.cn; keliang.zhou@whut.edu.cn).

Liangliang Lu is with the School of Integrated Circuit, Huazhong University of Science and Technology, Wuhan 430074, China, and also with the Lunar Exploration and Aerospace Engineering Center, State Administration for Science Technology and Industry for National Defence, Beijing 100190, China (e-mail: d202080855@hust.edu.cn).

Wei Song, Run Min, and Qiaoling Tong are with the School of Integrated Circuit, Huazhong University of Science and Technology, Wuhan 430074, China (e-mail: song_wei@hust.edu.cn; minrun@hust.edu.cn; tongqiaoling@hust.edu.cn).

Han Peng is with the School of Electrical and Electronic Engineering, Huazhong University of Science and Technology, Wuhan 430074, China (e-mail: pengh@hust.edu.cn).

Color versions of one or more figures in this article are available at https://doi.org/10.1109/TPEL.2023.3317910.

Digital Object Identifier 10.1109/TPEL.2023.3317910

TABLE I
COMPARISONS OF DIFFERENT CONTROL METHODS

Control method	Power flow	ZVS	Output voltage ripple	Extra power components
Conventional PFM	Continuous	Lost at light load	Low	None
Out-phasing [19], [20], [21]	Continuous	Yes	Low	Two inverter stages are required
Cycling-skipping [16], [17], [18]	Intermittent	Yes	Medium	One extra power switch is required
Conventional ON/OFF	Highly intermittent	Yes	High	None
VF ON/OFF [13]	Intermittent	Yes	Medium	None
MPL ON/OFF [14]	Intermittent	Yes	Medium	None
Zero-transient ON/OFF [15]	Intermittent	Yes	Low	Two extra power switches and two extra capacitors are required
Proposed method	Continuous	Yes	Low	None

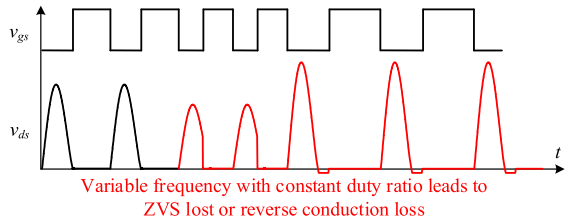

Fig. 1. Voltage waveforms of VHF class E DC–DC converter under conventional PFM.

large switching loss. For gallium nitride (GaN) high electron mobility transistor (HEMT)-based VHF power converters, deviated switching frequency would also cause increased reverse conduction loss when the switching frequency is below the optimal value. To reduce reverse conduction time of GaN HEMT, gate driver ICs with reverse conduction detection circuits are proposed in [24], [25], and [26]. The gate driver ICs can reduce the reverse conduction time regardless of operation conditions, but the maximum switching frequency is constrained by the detection circuit delay. Table I gives a comprehensive overview of advantages and disadvantages of existing control methods. Notably, none of these methods can realize continuous power flow while maintaining consistent ZVS without extra power components.

To reduce the output voltage ripple while maintaining consistent ZVS, this article proposes an optimal duty ratio assisted PFM based on a resonant fitting model for VHF isolated class E dc–dc converter. The proposed control features reduced output voltage ripple (owing to continuous power flow) and consistent ZVS without extra power components. Firstly, the rectifier is modeled as frequency-controlled inductor and resistor using descriptive function. Then, the resonant network is simplified with impedance fitting. Based on the simplified circuit model, the switching node voltage (v_{ds}) and output power (P_o) under dynamic switching frequency (f_s) are derived. Furthermore, the optimal duty ratio under dynamic switching frequency is calculated according to zero-crossing points of v_{ds}, assisting PFM to achieve minimized switching loss. The proposed control calculates the optimal duty ratio with the real-time switching frequency, so as to turn ON the power switch once v_{ds} reaches zero. It ensures ZVS and prevents reverse conduction of the power switch under dynamic switching frequency. Under light load, ON/OFF control is adopted to extend the load range. A 10–18 MHz prototype is built to verify effectiveness of the proposed control.

The rest of this article is organized as follows. Section II presents the resonant fitting model for VHF class E dc–dc converter. Section III proposes the optimal duty ratio assisted PFM control method. Section IV presents experimental results. Finally, Section V concludes this article.

II. RESONANT FITTING MODEL FOR VHF ISOLATED CLASS E DC–DC CONVERTER

A VHF isolated Class E dc–dc converter under closed-loop control is shown in Fig. 2. The converter consists of a class E inverter and a class E rectifier. The inverter stage is composed of resonant inductor L_k, magnetic inductance L_m, resonant capacitor C_F and power switch S, which converts dc input voltage into high frequency ac voltage. The rectifier is composed of resonant inductor L_R, resonant capacitor C_R and diode D_R, which converts the ac voltage back to dc. The output voltage is regulated by PFM control. Due to resonant nature of the converter, ZVS failure and reverse conduction may occur under dynamic switching frequency.

To realize ZVS and prevent reverse conduction of GaN HEMT, it is necessary to derive time-domain switching node voltage under dynamic switching frequency. However, since there are four states (due to on/off combination of S and D_R) and five resonant components (L_k, L_m, L_R, C_F, and C_R) in the circuit, it becomes very complicated to analyze the time-domain behavior directly.

To address above issue, this section proposes a resonant fitting model for VHF isolated class E dc–dc converter. The derivation process includes three steps, as shown in Fig. 3.

Step 1: Modeling the rectifier based on descriptive function. This step models the rectifier with frequency-controlled inductor and resistor, reducing the circuit states from 4 to 2 and reducing the resonant components from 5 to 4.

Step 2: Simplifying the resonant network with impedance fitting. This step fits impedance characteristics of the resonant tank, reducing the resonant components from 4 to 2.

Step 3: Deriving the optimal switch timing by solving the circuit model in time-domain.

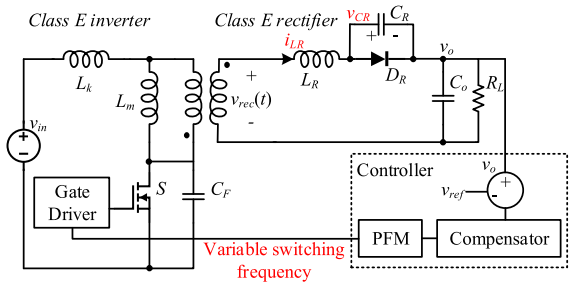

Fig. 2. VHF isolated class E DC–DC converter under closed-loop control.

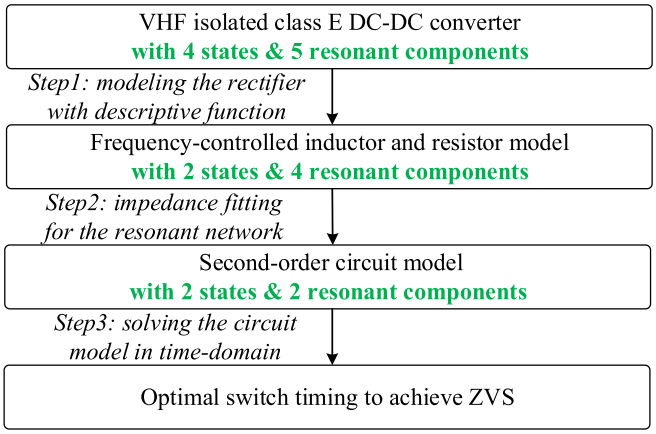

Fig. 3. Derivation process of the resonant fitting model and optimal switch timing.

A. Modeling the Rectifier With Descriptive Function

Since the rectifier is a nonlinear system, its characteristics highly rely on amplitude of the rectifier input voltage, which is controlled by switching frequency f_s. Conventional method usually models the rectifier as a resistor, which induces large error for time-domain analysis under dynamic switching frequency. On the other hand, direcT modeling with ON/OFF states of the diode are too complex for calculations. To address above issues, this sub-section models the rectifier as frequency-controlled inductor and resistor based on descriptive function, as shown in Fig. 4.

First, the input voltage of the rectifier is approximated as

$$v_{\mathrm{rec}}(t) = V_{\mathrm{rec}}(\omega_s)\sin(\omega_s t + \theta) \tag{1}$$

where $\omega_s = 2\pi f_{\mathrm{s}}$, f_{s} is the switching frequency and θ is the initial phase of $v_{\mathrm{rec}}(t)$. $V_{\mathrm{rec}}(\omega_s)$ is amplitude of the rectifier

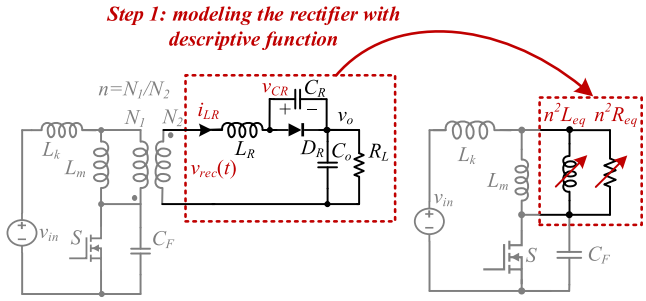

Fig. 4. Modeling the rectifier as frequency-controlled inductor and resistor with descriptive function.

input voltage, which can be calculated according to fundamental harmonic amplitude of the inverter output voltage.

When D_R is OFF, i_{LR} flows through C_R and the output network. Therefore, differential equations of i_{LR} and v_{CR} are as follows:

$$\begin{cases} L_R\frac{di_{LR}(t)}{dt} + v_{CR}(t) + v_o = V_{rec}(\omega_s)\sin(\omega_s t + \theta) \\ C_R\frac{dv_{CR}(t)}{dt} = i_{LR}(t) \end{cases}. \tag{2}$$

At $t = 0$, the diode turns OFF with ZCS. Therefore, these differential equations should meet the following boundary conditions: $v_{CR}(0) = v_D$, $i_{LR}(0) = 0$. Solving (2) with the boundary conditions yields (3) shown at the bottom of this page.

When D_R is on, i_{LR} flows through D_R and the output network. With a constant voltage drop of v_D, the differential equations are given by

$$\begin{cases} L_R\frac{di_{LR}(t)}{dt} + v_D + v_o = V_{rec}(\omega_s)\sin(\omega_s t + \theta) \\ v_{CR}(t) = v_D \end{cases}. \tag{4}$$

Solving (4) yields

$$\begin{cases} v_{CR}(t) = v_D \\ i_{LR}(t) = i_{LR}(t_{offrec}) - \frac{v_o+v_D}{L_R}(t - t_{offrec}) \\ \quad + \frac{V_{rec}(\omega_s)(\cos(\omega_s t_{offrec}+\theta) - \cos(\omega_s t+\theta))}{L_R\omega_s} \end{cases} \tag{5}$$

where t_{offrec} is the time duration when the diode is OFF. Both t_{offrec} and θ are unknown parameters, and they are determined by boundary conditions in the followings. The diode turns ON at $t = t_{\mathrm{offrec}}$, (b) the inductor current is periodic, i.e.,

$$\begin{cases} v_{CR}(t_{\mathrm{offrec}}) = v_D \\ i_{LR}(0) = i_{LR}(T) \end{cases}. \tag{6}$$

Furthermore, descriptive function of the rectifier is derived based on Fourier analysis. Resistive component ($i_{LR,\ \mathrm{res}}$) and

$$\begin{cases} v_{CR}(t) = \dfrac{\left(\begin{array}{l} V_{rec}(\omega_s)C_R\omega_s\cos(\theta)\cos(\frac{t}{\sqrt{C_RL_R}}) - V_{rec}(\omega_s)C_R\omega_s\cos(\omega_s t+\theta) \\ +\sqrt{\frac{C_R}{L_R}}\left((v_o+v_D)(1-C_RL_R\omega_s^2) - V_{rec}(\omega_s)\sin(\theta)\right)\sin(\frac{t}{\sqrt{C_RL_R}}) \end{array}\right)}{(-1+C_RL_R\omega_s^2)} \\ i_{LR}(t) = -v_o + (v_o+v_D)\cos(\frac{t}{\sqrt{C_RL_R}}) + \frac{-V_{rec}(\omega_s)\sin(\omega_s t+\theta)}{-1+C_RL_R\omega_s^2} \\ \quad + \dfrac{V_{rec}(\omega_s)\cos(\frac{t}{\sqrt{C_RL_R}})\sin(\theta) + V_{rec}(\omega_s)\sqrt{C_RL_R}\omega_s\sin(\frac{t}{\sqrt{C_RL_R}})\cos(\theta)}{(-1+C_RL_R\omega_s^2)} \end{cases}. \tag{3}$$

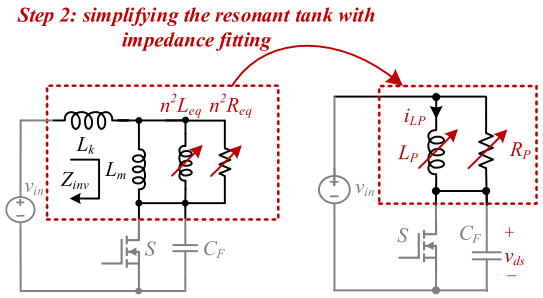

Fig. 5. Simplifying the resonant network with impedance fitting.

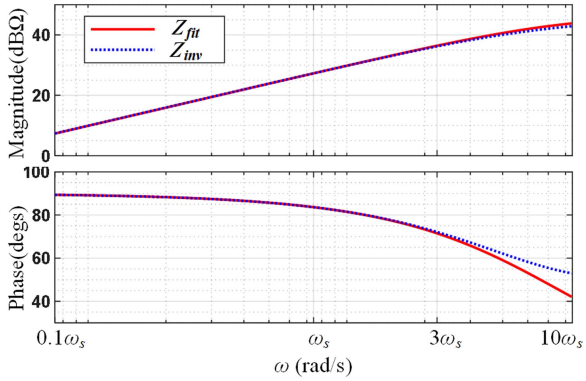

Fig. 6. Bode plot of $Z_{\text{inv}}(j\omega)$ and $Z_{\text{fit}}(j\omega)$, where $L_k = 72$ nH, $L_m = 353$ nH, $R_{\text{eq}} = 8.9\ \Omega$, $L_{\text{eq}} = 55$ nH, $n = 4$, $R_P = 208.7\ \Omega$, $L_P = 312.8$ nH, and $\omega_s = 2\pi{\cdot}11.8{\cdot}10^6$.

inductive component ($i_{LR,\ \text{ind}}$) of the rectifier input current are calculated as

$$\begin{cases} i_{LR,\text{res}} = \frac{2}{T}\int_0^T i_{LR}(t)\sin(\omega_s t+\theta)dt \\ i_{LR,\text{ind}} = \frac{2}{T}\int_0^T -i_{LR}(t)\cos(\omega_s t+\theta)dt \end{cases}. \tag{7}$$

With the resistive and inductive current in (7), the rectifier can be modeled by frequency-controlled resistor $R_{\text{eq}}(\omega_s)$ and inductor $L_{\text{eq}}(\omega_s)$. Therefore, descriptive function of the rectifier is given by (8). Furthermore, considering the transformer turn ratio n, the VHF class E dc–dc converter is simplified as shown in Fig. 4.

$$\begin{cases} R_{\text{eq}}(\omega_s) = \frac{V_{\text{rec}}(\omega_s)}{i_{LR,\text{res}}} \\ L_{\text{eq}}(\omega_s) = \frac{V_{\text{rec}}(\omega_s)}{\omega_s i_{LR,\text{ind}}} \end{cases}. \tag{8}$$

B. Impedance Fitting for the Resonant Network

The switching node voltage is mainly determined by fundamental characteristics of the resonant network $Z_{\text{inv}}(j\omega)$. By fitting $Z_{\text{inv}}(j\omega)$ at ω_s with a simple network, the calculation can be further reduced. In the followings, characteristic of the resonant tank is fitted with R_P and L_P as shown in Fig. 5. The principle is based on the fact that $Z_{\text{inv}}(j\omega)$ is inductive at low frequency and becomes resistive at high frequency.

In Fig. 5, impedance of the original resonant network is calculated as

$$Z_{\text{inv}}(j\omega) = j\omega L_k + \frac{1}{\frac{1}{j\omega L_m} + \frac{1}{j\omega n^2 L_{\text{eq}}} + \frac{1}{n^2 R_{\text{eq}}}}. \tag{9}$$

To simplify the network, an impedance fitting function is given by (10), which is constructed by a pair of inductor and resistor in parallel

$$Z_{\text{fit}}(j\omega) = \frac{1}{\frac{1}{R_P} + \frac{1}{j\omega L_P}}. \tag{10}$$

To achieve impedance fitting, $Z_{\text{fit}}(j\omega)$ and $Z_{\text{inv}}(j\omega)$ should be equal at ω_s, i.e.,

$$Z_{\text{fit}}(j\omega_s) = Z_{\text{inv}}(j\omega_s). \tag{11}$$

Combining (9)–(11), the fitting parameters R_P and L_P are calculated as

$$\begin{cases} L_P = \frac{R_S^2}{L_S\omega_s^2} + L_S,\ R_P = R_S + \frac{L_S^2\omega_s^2}{R_S} \\ L_S = L_k + \frac{n^4 L_{\text{eq}} R_{\text{eq}} L_m (n^2 L_{\text{eq}} R_{\text{eq}} + L_m R_{\text{eq}})}{(n^3 L_{\text{eq}} R_{\text{eq}} + n L_m R_{\text{eq}})^2 + (\omega_s n L_m L_{\text{eq}})^2} \\ R_S = \frac{n^4\omega_s^2 R_{\text{eq}} L_{\text{eq}}^2 L_m^2}{(n^3 L_{\text{eq}} R_{\text{eq}} + n L_m R_{\text{eq}})^2 + (\omega_s n L_m L_{\text{eq}})^2} \end{cases}. \tag{12}$$

A fitting example is plotted in Fig. 6, which shows the fitting result matches Z_{inv} well from 0.1 ω_s to 3 ω_s. By fitting the resonant network with R_P and L_P, the VHF class E dc–dc converter is simplified as a second-order model, which is convenient to solve.

C. Deriving the Optimal Switch Timing to Achieve ZVS

With the impedance fitting model in Fig. 5, this section derives the optimal switch timing to achieve ZVS based on time-domain description of the circuit.

During $0 \le t \le t_{\text{offinv}}$, the power switch is OFF, and the circuit satisfies the following differential equations:

$$\begin{cases} L_P \frac{di_{LP}(t)}{dt} + v_{ds}(t) = v_{\text{in}} \\ C_F \frac{dv_{ds}(t)}{dt} = i_{LP}(t) + \frac{v_{\text{in}} - v_{ds}(t)}{R_P} \end{cases}. \tag{13}$$

The power switch turns OFF at $t = 0$, and turns ON at $t = t_{\text{offinv}}$ with ZVS. Therefore, these differential equations should meet the following boundary conditions: $v_{ds}(0) = 0$ and $v_{ds}(t_{\text{offinv}}) = 0$. Solutions of (13) are given by

$$\begin{cases} v_{ds}(t) = v_{\text{in}} + c_1 e^{(-\alpha-\beta)t} + c_2 e^{(-\alpha+\beta)t} \\ i_{LP}(t) = \frac{\begin{pmatrix} c_2 e^{(-\alpha+\beta)t}(1 - \alpha C_F R_P + \beta C_F R_P) \\ -c_1 e^{(-\alpha-\beta)t}(-1 + \alpha C_F R_P + \beta C_F R_P) \end{pmatrix}}{R_P} \end{cases} \tag{14}$$

where α, β, c_1, and c_2 are calculated as

$$\begin{cases} \alpha = \frac{1}{2C_F R_P},\ \beta = \frac{\sqrt{L_P - 4C_F R_P^2}}{2C_F R_P \sqrt{L_P}} \\ c_1 = \frac{v_{\text{in}}(1 - e^{(-\alpha+\beta)t_{\text{offinv}}})}{(e^{(-\alpha+\beta)t_{\text{offinv}}} - e^{(-\alpha-\beta)t_{\text{offinv}}})},\ c_2 = \frac{v_{in}(e^{(-\alpha-\beta)t_{\text{offinv}}} - 1)}{(e^{(-\alpha+\beta)t_{\text{offinv}}} - e^{(-\alpha-\beta)t_{\text{offinv}}})} \end{cases}. \tag{15}$$

TABLE II
IMPLEMENTATION OF THE PROTOTYPE

Parameters	Value
v_{in}	28 V
v_o	5 V
P_o	10 W
f_s	10–18 MHz
L_k	65.3 nH
L_m	358.6 nH
L_R	65 nH
N_2:N_1	4
C_F	220 pF
C_R	1.8 nH
C_o	60.3 μF
Switch	EPC2207
Gate driver	UCC27611
Diode	2 PMEG45A10EPD in parallel
Main controller	STM32F334C8T6

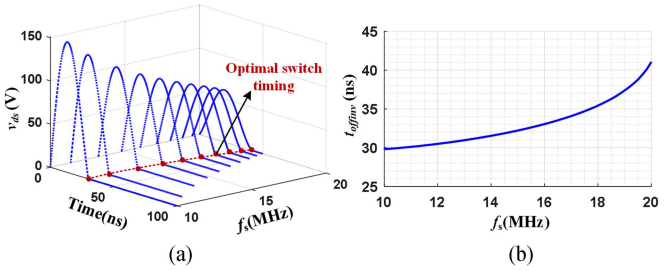

Fig. 7. Calculation results of $v_{ds}(t)$ and t_{offinv}. (a) Waveforms of v_{ds}(t) under dynamic f_s. (b) t_{offinv} with respect to f_s.

During $t_{\text{offinv}} < t \leq T$, the power switch is ON. Since R_P is much higher than ON-resistance of the power switch, $v_{ds}(t)$ is approximated as 0 during the switch-ON state. Thus, the current through R_P is given by v_{in}/R_P, and the current through L_P is given by $i_{LP}(t) = i_{LP}(t_{\text{offinv}}) + v_{\text{in}} \cdot (t\text{-}t_{\text{offinv}})/L_P$. At steady state, the inductor current is periodic, i.e., $i_{LP}(0) = i_{LP}(T)$. With this boundary condition, t_{offinv} is calculated. To verify effectiveness of the proposed resonant fitting model, the modeling results are compared with experimental results, which are provided in Appendix A. According to the results, the proposed model can predict the zero-crossing points precisely, so that to provide the correct timing to achieve ZVS.

Furthermore, a calculation example is carried out. The circuit parameters are the same as experiments, which are given by Table II in Section IV. Fig. 7(a) plots waveforms of $v_{ds}(t)$ under dynamic switching frequency. To achieve ZVS and prevent reverse conduction of GaN HEMT, the optimal timing for turning ON the power switch is when $v_{ds}(t)$ reaches zero (t_{offinv}). Fig. 7(b) plots t_{offinv} with respect to the switching frequency. Above results present time-domain description for the converter, which provides theoretical foundations for the proposed control.

III. Optimal Duty Ratio Assisted PFM for VHF Isolated Class E DC–DC Converter

Based on the simplified circuit model, this section proposes the optimal duty ratio assisted PFM control. The overall control schema is shown in Fig. 8. A PI compensator is used to control switching frequency of the power converter. To maintain ZVS under dynamic switching frequency, the optimal duty ratio is determined according to the real-time switching frequency. Furthermore, ON/OFF control is used at light load to extend load range of the power converter.

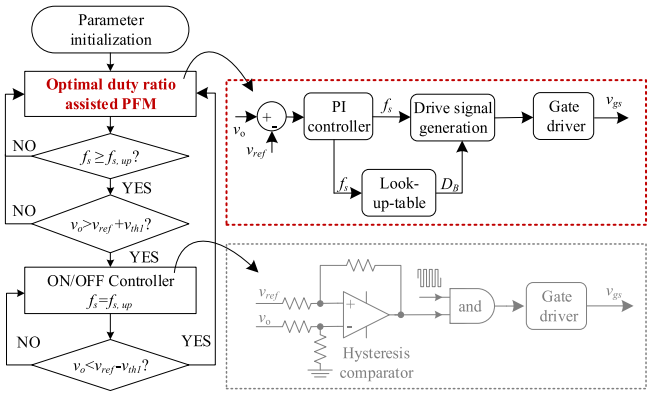

Fig. 8. Overall schema of the proposed optimal duty ratio assisted PFM controller.

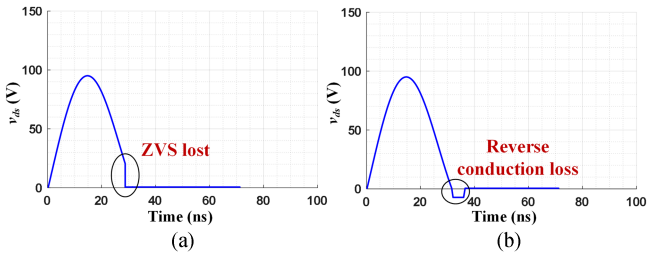

Fig. 9. Switch voltage with nonoptimal duty ratio. (a) Large duty ratio leads to ZVS failure. (b) Small duty ratio leads to high reverse conduction loss.

A. Optimal Duty Ratio and Output Power Under Dynamic Switching Frequency

For VHF power converters, it is essential to achieve ZVS, otherwise, the power efficiency would drop dramatically. Additionally, reverse conduction voltage of GaN HEMT is large, hence, long reverse conduction time leads to high reverse conduction loss.

To improve power efficiency, it is important to turn ON the GaN HEMT with good timing. Generally, a large duty ratio leads to ZVS failure as shown in Fig. 9(a), whereas a small duty ratio leads to reverse conduction loss, as shown in Fig. 9(b). To achieve the optimal timing under dynamic switching frequency, the optimal duty ratio is derived with zero-crossing points of the power switch voltage. Analytical expression of the switching node voltage is derived in Section II-C. By solving

$$v_{ds}(t) = 0 \tag{16}$$

zero-crossing points of the switching node voltage are given by $t = 0$ and $t = t_{\text{offinv}}$, as shown in Fig. 10(a). Therefore, the

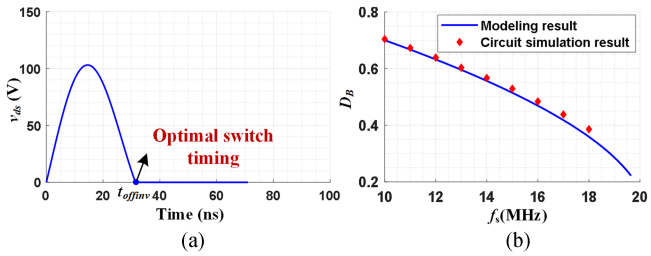

Fig. 10. $v_{ds}(t)$ with optimal switch timing and optimal duty ratio with respect to f_s. (a) $v_{ds}(t)$ with optimal switch timing. (b) Optimal duty ratio with respect to f_s.

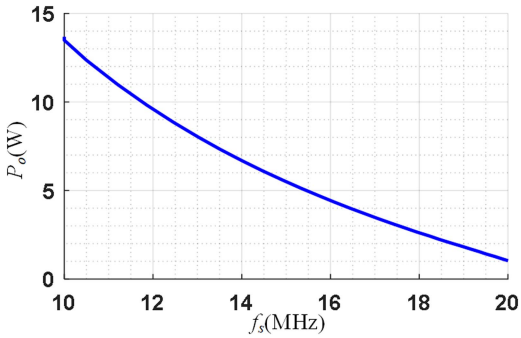

Fig. 11. Output power with respect to the switching frequency.

optimal duty ratio is calculated as

$$D_B = \frac{T - t_{\text{offinv}}}{T}. \tag{17}$$

The optimal duty ratio decreases as the switching frequency increases as shown in Fig. 10(b). With the result, the optimal duty ratio can be calculated with the real-time switching frequency, which ensures ZVS without inducing reverse conduction loss of GaN HEMT.

Output power of the converter is calculated as

$$P_{\text{o}} = \frac{v_R i_{LR,\text{res}}}{2} = \frac{v_R^2}{2R_{\text{eq}}}. \tag{18}$$

Increasing the switching frequency leads to decreased v_R and increased R_{eq}. Thus, the output power decreases monotonically with the switching frequency, as shown in Fig. 11. Detailed analysis for the relationship between P_o and f_s can be found in [13]. Therefore, it is possible to regulate the output voltage by controlling the switching frequency with a feedback controller, which provides foundations for the proposed control method.

B. Implementation of the Optimal Duty Ratio Assisted PFM

Implementation of the proposed control is shown in Fig. 8. The optimal duty ratio assisted PFM controller adjusts the switching frequency f_s according to the output voltage error. The optimal duty ratio is precalculated and stored in a look-up-table. The proposed controller selects the optimal duty ratio D_B according to the real-time switching frequency f_s. Then, D_B and f_s determine the gate driving signal together.

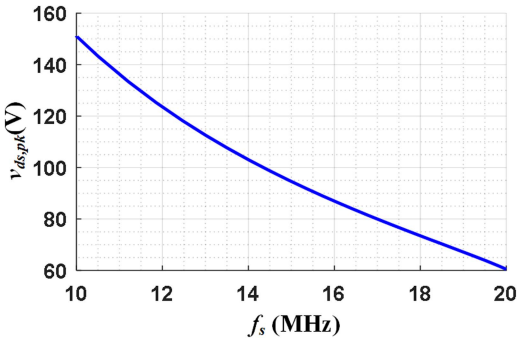

Fig. 12. Switch voltage stress with respect to the switching frequency.

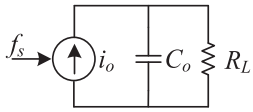

Fig. 13. Small signal model of the main power stage.

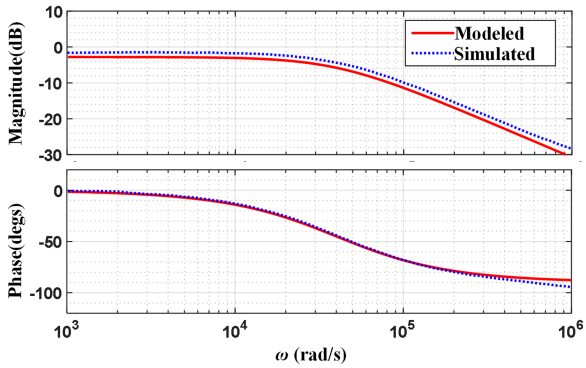

Fig. 14. Comparison of modeling result and simulation result of G_{vf}(s).

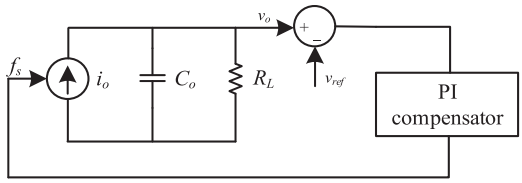

Fig. 15. Small signal of the converter under proposed control.

In a practical class E dc–dc converter, the switching frequency range is limited by voltage stress and switching speed of the power switch. Lower limit of the switching frequency is determined by the switch voltage stress. Fig. 12 shows the switch voltage stress $v_{ds,pk}$ with respect to the switching frequency f_s. As the switching frequency decreases, the peak switch voltage increases. Additionally, due to the nonlinear output capacitance of the power switch, the peak switch voltage in real system is larger than the calculated value. To guarantee the power switch operates in safe operating area, the lower frequency boundary is set as 10 MHz.

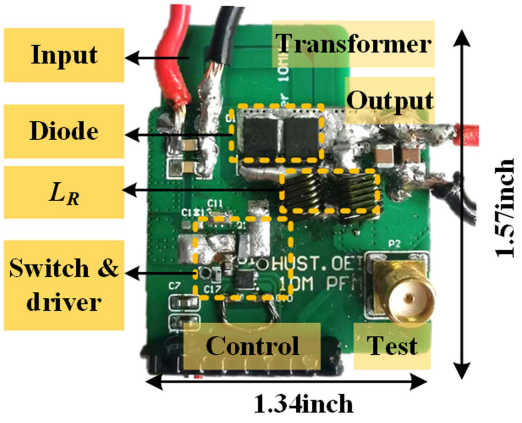

Fig. 16. Prototype of the VHF isolated class E DC–DC converter.

Upper limit of switching frequency ($f_{s,\mathrm{up}}$) is determined by the switching speed. As the switching frequency increases, the optimal duty ratio and conduction time decrease. It is hard to realize reliable gate drive when the turn-ON time is too short. To realize reliable gate drive, the upper switching frequency limit is set as 18 MHz. At light load (smaller than 30%), the optimal duty ratio assisted PFM cannot regulate the output voltage to v_{ref} due to upper limit of the switching frequency. To address this issue, ON/OFF control is used to regulate the output voltage at light load as shown in Fig. 8.

C. Close Loop Stability of the Converter

The followings provide small signal analysis for VHF isolated class E dc–dc converter under the proposed control scheme. First, the main power stage is modeled as a frequency-controlled current source as shown in Fig. 13.

Based on Fig. 13, the transfer function from f_s to v_o is given by (19), where $G_{if}(s)$ is the transfer function from f_s to i_o, R_L is the load resistor and C_o is the output capacitor

$$G_{vf}(s) = G_{if}(s)\frac{R_L}{1+sR_LC_o} \approx G_{if}(0)\frac{R_L}{1+sR_LC_o}. \quad (19)$$

For VHF resonant power converters, the resonant inductors and capacitors are very small, zeros and poles of $G_{if}(s)$ are much higher than the system bandwidth. Therefore, $G_{if}(s)$ can be approximated with its dc gain $G_{if}(0)$, which is calculated as

$$G_{if}(0) = \frac{\partial i_o}{\partial f_s} = \frac{\partial\sqrt{P_o/R_L}}{\partial f_s} = \frac{1}{2}\sqrt{\frac{1}{R_LP_o}}\frac{\partial P_o}{\partial f_s} = \frac{1}{2v_o}\frac{\partial P_o}{\partial f_s}. \quad (20)$$

Value of $\partial P_o/\partial f_s$ is calculated according to slope of the curve in Fig. 11. To ensure stability of the system, the maximum slope is used as $G_{if}(0)$, where $\partial P_o/\partial f_s$ = -2.9 W/MHz and $G_{if}(0)$ = -0.29 A/MHz. To verify the proposed small signal model, simulations are carried out in MATLAB/Simulink. Fig. 14 shows the modeling result of $G_{vf}(s)$ matches the simulation result well. Thus, the small signal model can be used to guide control loop design.

Small signal model of the converter under proposed control is shown in Fig. 15.

Based on Fig. 15, loop gain of the system is given by

$$\Phi_{LP}(s) = G_{vf}(s)G_{pi}(s) = \frac{G_{if}(0)R_Lk_p}{sR_LC_o}\frac{s+k_i/k_p}{s+1/R_LC_o} \quad (21)$$

where $G_{pi}(s)$ is transfer function of the PI compensator and k_p and k_i are proportion and integration coefficient of the PI compensator. Furthermore, k_i/k_p is set to cancel dominate pole of the system, while k_p is set to obtain desired bandwidth ω_n. With above conditions, k_p and k_i are given by $k_p = \omega_nC_o/G_{if}(0)$, $k_i = \omega_n/(G_{if}(0)R_L)$. With the calculated parameters, loop gain of the system is given by (22), which is a single-pole system

$$\Phi_{LP}(s) = \frac{G_{if}(0)R_Lk_p}{sR_LC_o}. \quad (22)$$

The single-pole characteristic indicates that the system is stable and has a phase margin of 90° under the proposed control.

IV. Experimental Results

To verify effectiveness of the proposed control method, a VHF isolated class E dc–dc converter is built as shown in Fig. 16. Main specifications of the converter are given in Table II. The input voltage is 28 V, the output voltage is 5 V, the rated output power is 10 W, and the switching frequency is 10–18 MHz. The main power switch is GaN HEMT EPC2207, the diode is PMEG45A10EPD from Nexperia. The gate driver is realized with UCC27611, which is a high-speed gate driver from Texas Instruments. The gate driver is placed closely to the GaN HEMT, so as to provide reliable gate drive. Air core transformer and inductors are utilized owing to their eliminated core loss and great frequency linearity. The air core transformer is realized with a 4-layer print circuit board, which is mounted on back side of the board to reduce the size. The transformer characteristics acquired from impedance analyzer are provided in Appendix B. The resonant inductor L_R is implemented with two parallel-connected commercial air-core inductors from Coilcraft (2929SQ-131, 130 nH).

To generate precise gate driving signals from f_s and D_B, an MCU(STM32F334C8T6) with internal high-resolution timer is utilized, where the time resolution is 217 ps. Output voltage sampling is realized with the internal Adc in MCU. The sampling and PI calculation frequency is set as 100 kHz, which is much lower than the switching frequency (10–18 MHz). To decouple the mismatch between switching frequency and control frequency, the optimal duty ratios under different switching frequencies are pre-calculated based on the proposed resonant fitting model and stored in the digital controller. The proposed controller selects the optimal duty ratio (D_B) according to the real-time switching frequency (f_s).

A. Steady-State Operations

Waveforms of v_{ds} and v_{gs} with the proposed control method are shown in Fig. 17. At 100% load, the switching frequency is 12.1 MHz, and the optimal duty ratio is 0.63. With the proposed optimal duty ratio, the power switch is turned ON immediately once the switching node voltage reaches zero, which realizes ZVS with no reverse conduction loss induced. At 40% load, the

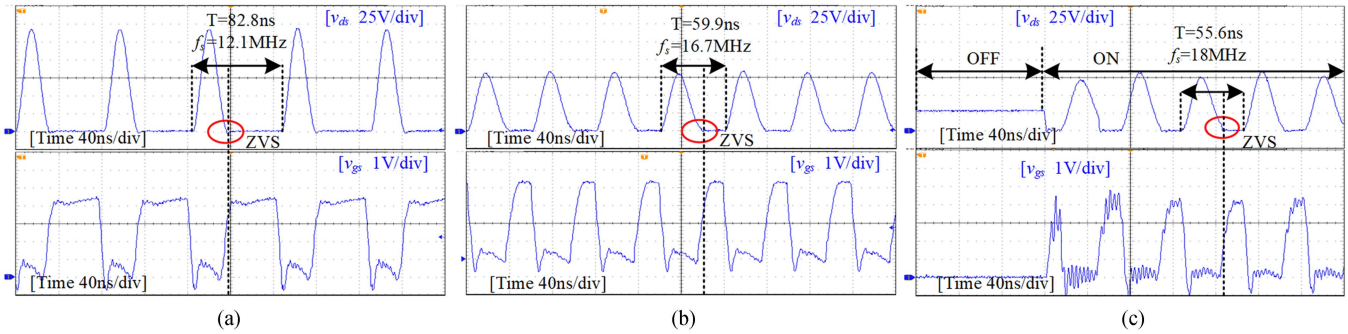

Fig. 17. v_{ds} and v_{gs} waveforms with the proposed control under different load. (a) 100% load. (b) 40% load. (c) 20% load.

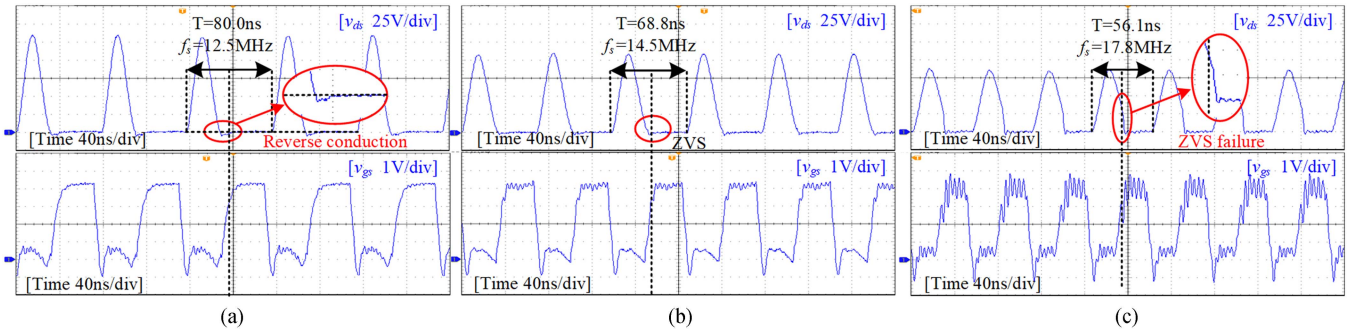

Fig. 18. v_{ds} and v_{gs} waveforms under conventional PFM with fixed duty ratio. (a) 100% load. (b) 60% load. (c) 40% load.

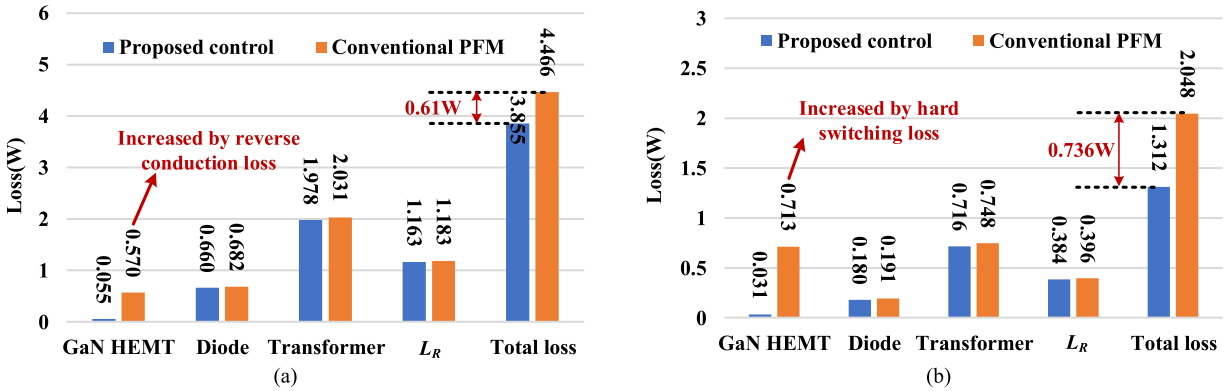

Fig. 19. Loss breakdown of the converter under different load and different control methods. (a) 100% load. (b) 40% load.

switching frequency is increased to 16.7 MHz, so that to reduce the output power and regulate the output voltage to 5 V. The duty ratio is adjusted to 0.39 according to the switching frequency, which guarantees ZVS without inducing reverse conduction loss. At 20% load, the converter enters ON/OFF control mode due to upper limit of the switching frequency.

Waveforms of v_{gs} and v_{ds} under conventional PFM with duty ratio fixed to 0.5 are shown in Fig. 18. At 100% load, the switching frequency is lower than the optimal value. With the duty ratio fixed to 0.5, the power switch is turned on 10.4 ns after the switching node voltage reaches zero, which causes large reverse conduction loss. At 60% load, the switching frequency equals the optimal value, which realizes ZVS without inducing reverse conduction loss. At 40% load, the switching frequency is higher than the optimal value, which leads to ZVS failure. The reverse conduction loss and ZVS failure can cause severe efficiency drop. Comparatively, the proposed optimal duty ratio assisted PFM can guarantee ZVS under dynamic switching frequency.

Fig. 19 shows loss breakdown of the converter under different control methods. The loss breakdown results are obtained based on LTspice simulations. The power switch and diode used in the simulations are level-3 SPICE models provided by the manufacturer. Parasitic resistances of the transformer and inductor are considered in the simulation, which are measured with LCR meter and then adopted in the simulations. Losses of the power

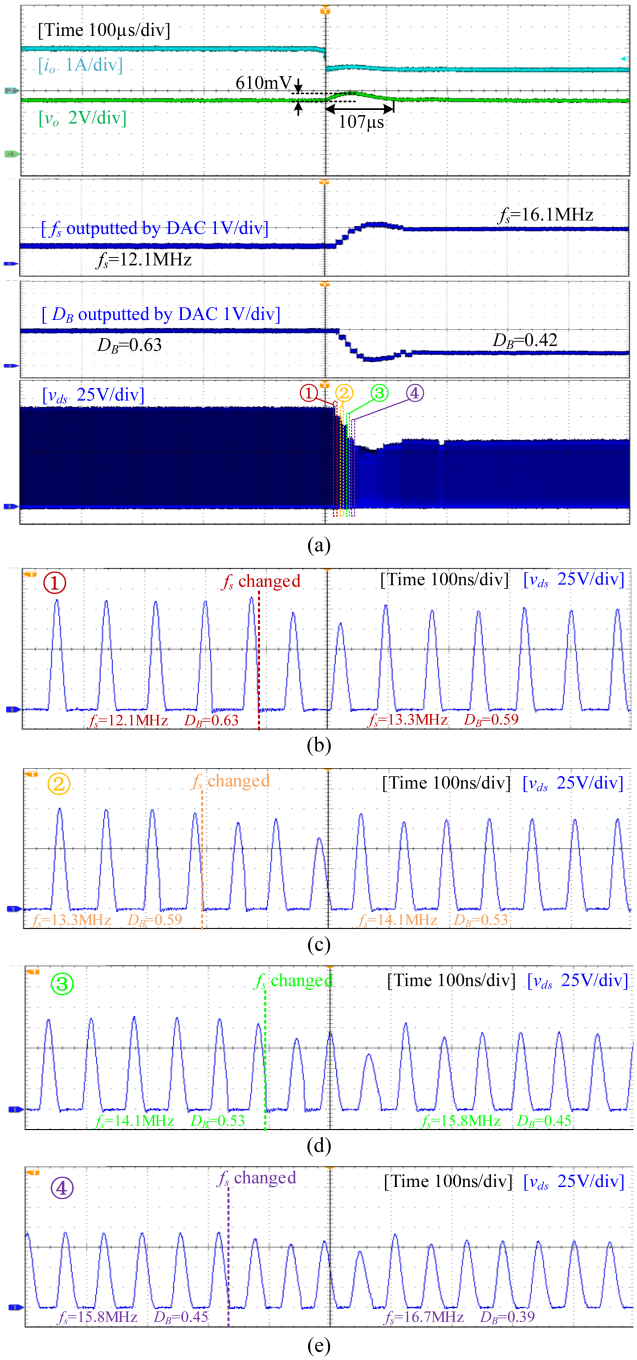

Fig. 20. Transient waveforms when load current steps from 100% to 50%. (a) waveforms of i_o, v_o, v_{ds}, f_s, and D_B. (b) Detailed v_{ds} in area ①. (c) Detailed v_{ds} in area ②. (d) Detailed v_{ds} in area ③. (e) Detailed v_{ds} in area ④.

switch and diode are obtained by calculating the average value of voltage-current products at the device terminals. Losses of the transformer and inductor are calculated according to the parasitic resistances and root mean square values of branch currents. Parasitic resistance of the transformer primary coil is 0.36 Ω, parasitic resistance of the transformer secondary coil is 0.04 Ω, and parasitic resistance of the resonant inductor is 0.1Ω. At 100% load, the proposed control reduces the total loss by 0.61 W (13.7% reduction). This is because the proposed control method prevents reverse conduction of GaN HEMT with the optimal switch timing. At 40% load, the proposed control reduces the total loss by 0.736 W (35.9% reduction), which is because the proposed method ensures ZVS with the optimal duty ratio under dynamic switching frequency.

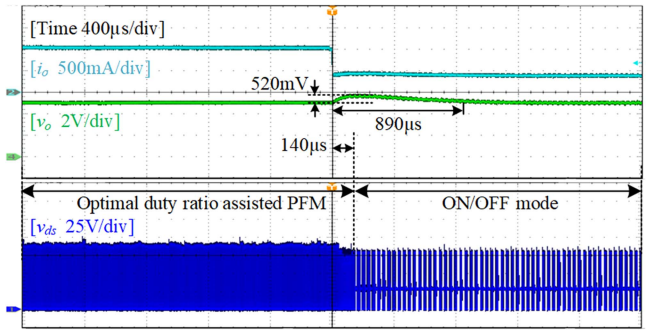

Fig. 21. Transient waveforms of i_o, v_o, and v_{ds} when load current steps from 50% to 20%.

B. Transient Responses

Fig. 20(a) shows the waveforms of i_o, v_o, and v_{ds} when the load current steps from 100% to 50%. The f_s value is mapped from 10–18 MHz to 0–3.3 V analog signal, while the D_B value is mapped from 0.26–0.7 to 0–3.3 V analog signal with internal DAC of STM32F334C8T6. After the load step, the feedback loop gradually increases f_s from 12.1 to 16.1 MHz, which reduces the output power so that to regulate the output voltage to 5 V. In the meanwhile, D_B is reduced from 0.63 to 0.42, so as to maintain ZVS of the power switch. Fig. 20(b)–(e) are the detailed v_{ds} waveforms in areas ①, ②, ③, and ④ of Fig. 20(a), respectively. In Fig. 20(b), f_s changes from 12.1 to 13.3 MHz, and D_B changes from 0.63 to 0.59 that achieves ZVS. In Fig. 20(c)–(e), the measured f_s gradually changes from 13.3 to 16.7 MHz. In all transients, D_B changes simultaneously with f_s, while ZVS of the power switch is recovered within three switching cycles after f_s changes.

In Fig. 21, the load current steps from 50% to 20%. The power converter initially operates in optimal duty ratio assisted PFM control. After 140 μs, the switching frequency reaches its upper limit, and controller changes the control mode to ON/OFF control. The voltage overshoot is 520 mV, and the settling time is 890 μs.

C. Power Efficiency and Output Voltage Ripple

Fig. 22(a) shows power efficiency comparison among the proposed control, conventional PFM, and ON/OFF control. When $i_o = 1.2$ A, power efficiency of the proposed method and conventional PFM are both 75.1%. When i_o is smaller than 1.2 A, ZVS failure causes severe efficiency drop under conventional PFM. When i_o is larger than 1.2 A, the reverse conduction loss under conventional PFM degrades the power efficiency. The conventional PFM lost ZVS at light load, which highly degrades the efficiency. Comparatively, the proposed method can

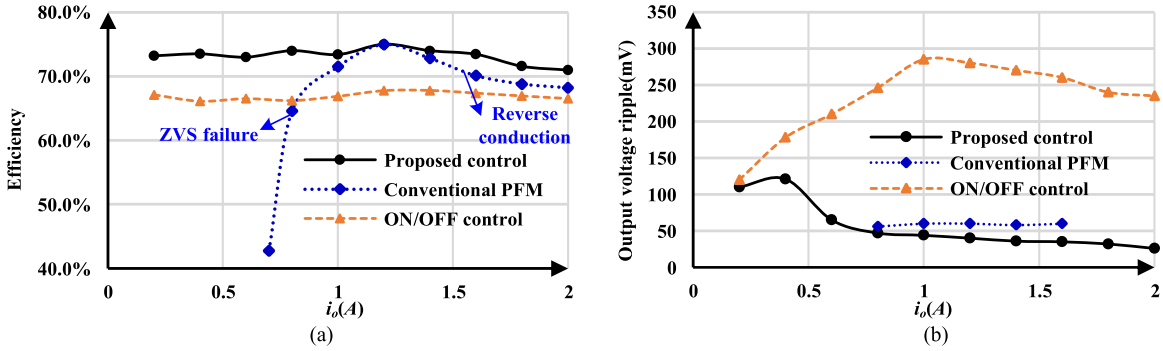

Fig. 22. Output voltage ripple and power efficiency. (a) Power efficiency. (b) Output voltage ripple.

TABLE III
COMPARISONS WITH OTHER CONTROL METHODS

Control method	Input voltage	Output voltage/power	Switching frequency	Efficiency	Output ripple	Output capacitor	Extra power components	FOM_{ripple}
Proposed control method	28 V	5 V/10 W	12–18 MHz	75%	26 mV	60.3 μF	None	**9.4-14.1 V·μF·MHz/A**
Zero-transient ON/OFF [15]	5 V	10 V/1 W	4–8 MHz	73%	20 mV	20 μF	Two extra power switch and Two extra capacitors	16–32 V·μF·MHz/A
Multipower level ON/OFF [14]	18 V	5 V/10 W	19.6–23.5 MHz	75%	100 mV	100 μF	None	98–117.5 V·μF·MHz/A
Variable frequency ON/OFF [13]	18 V	5 V/10 W	20–25 MHz	74%	150 mV	40 μF	None	60–75 V·μF·MHz/A
Conventional ON/OFF [8], [9]	24 V	5 V/10 W	30 MHz	75%	180 mV	10.8 μF	None	29.2 V·μF·MHz/A
	5 V	5 V/2 W	30 MHz	79%	220 mV	20 μF	None	330 V·μF·MHz/A

guarantee ZVS without inducing reverse conduction loss over the whole load range, thus achieving higher power efficiency than conventional PFM. Additionally, the proposed method can reduce circling current of the resonant tank with dynamic switching frequency, thus achieving higher efficiency than ON/OFF control.

Fig. 22(b) shows output voltage ripple comparison of the proposed control, conventional PFM, and ON/OFF control. At 100% load, the proposed control method significantly reduces the output voltage ripple to 26 mV. For fair comparison of ripple, a figure of merit (FOM) is defined as (23), which takes the factors of output filter capacitor, output current, and switching frequency into consideration [27], [28]

$$\mathrm{FOM}_{\mathrm{ripple}} = \frac{\Delta v_o C_o f_s}{i_o}. \tag{23}$$

Table III gives detailed comparisons of different control methods. Although ON/OFF control can realize ZVS regardless of load conditions, the intermittent power flow under ON/OFF control causes large output voltage ripple and mode transition losses. Compared with existing controls, the proposed optimal duty ratio assisted PFM is the first control method that features reduced output ripple (owing to continuous power flow) and consistent ZVS.

V. CONCLUSION

This article proposed an optimal duty ratio assisted PFM for very high frequency (VHF) isolated class E DC-DC converter. It is the first control method that features continuous power flow and consistent ZVS without extra power components. A resonant fitting model is established with descriptive function and impedance fitting, which provides time-domain analysis for the converter. Furthermore, an optimal duty ratio assisted PFM control is proposed, which turns ON the power switch with the optimal timing. This control ensures ZVS and prevents reverse conduction of GaN HEMT under dynamic switching frequency. Experimental results show that the proposed method improves the overall power efficiency over a wide load range. Additionally, since the power converter operates continuously, the output voltage ripple is significantly reduced. The optimized power loss and ripple can reduce the requirement of heat sink and output capacitor, which are beneficial to improve power density of the system. However, limited by calculation delay of the digital controller, dynamic response of the proposed control is slower than ON/OFF control.

APPENDIX A

This appendix is provided to demonstrate effectiveness of the proposed resonant fitting model. The experimental v_{ds} waveforms and data are measured with oscilloscope MDO3054.

TABLE IV
DEVIATIONS OF V_{ds} AND DUTY RATIO COMPARED WITH EXPERIMENTAL RESULTS AFTER EACH MODELING AND FITTING STEP

	Deviation of v_{ds}	Deviation of duty ratio
Step 1: modeling the rectifier	Nonevident	0.74%
Step 2: impedance fitting	Nonevident	0.85%
Step 3: solving the differential equations	Evident	0.49%

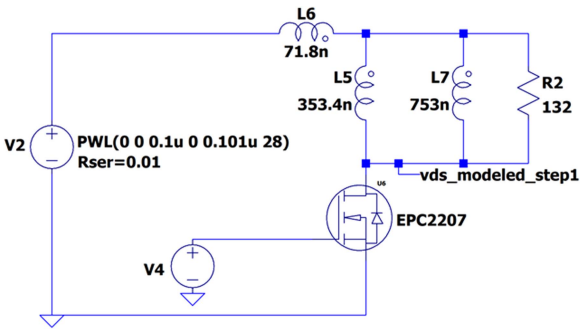

Fig. 23. Circuit model after modeling the rectifier as parallel-connected inductor (L7) and resistor (R2).

Then, the measured data is imported to LTspice as piece-wise linear (PWL) file. Furthermore, the experimental and modeling results are plotted in the same figure with LTspice to compare the waveforms. Table IV summarizes deviations of modeled v_{ds} and duty ratio compared with the experimental results. According to the results, deviations of v_{ds} and duty ratio caused by step 1(modeling the rectifier) and step 2 (impedance fitting) are nonevident. Step 3 causes evident deviation of v_{ds} waveform due to nonlinear output capacitance of the power switch. Despite of the deviated waveform, the proposed model can still predict the duty ratio precisely owing to the use of charge-based equivalent capacitance, so that provides correct timing to achieve ZVS. Detailed comparisons are presented as followings.

A. Step 1: Modeling the Rectifier With Inductor and Resistor

Fig. 23 shows the circuit model after modeling step 1, where the rectifier is modeled as parallel-connected inductor (L7) and resistor (R2). The experimental and modeled v_{ds} waveforms are shown in Fig. 24. Difference between the v_{ds} waveforms is relatively small, and zero-crossing points of the v_{ds} waveforms are almost the same. Therefore, after this modeling step, the derived v_{ds} waveform can provide correct switch timing to achieve ZVS.

B. Step 2: Impedance Fitting to Reduce Order of the Resonant Network

To further simplify the calculations, order of the resonant network is reduced based on impedance fitting. Fig. 25 shows the circuit model after impedance fitting. Fig. 26 compares the

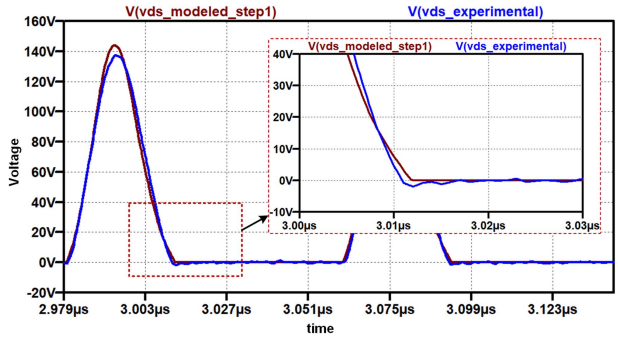

Fig. 24. Comparison of modeled v_{ds} after step 1 with experimental v_{ds}.

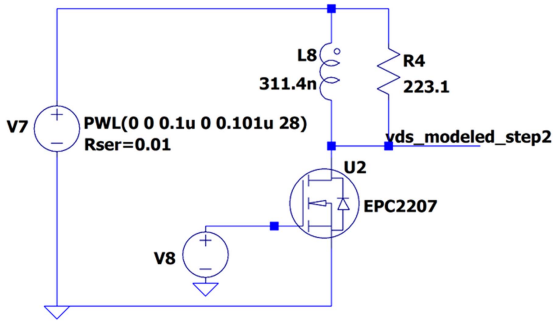

Fig. 25. Circuit model after impedance fitting.

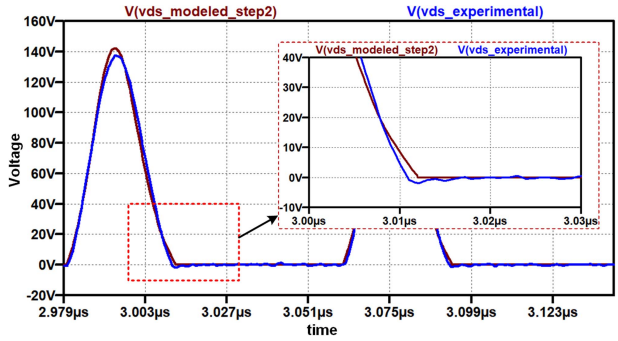

Fig. 26. Comparison of modeled v_{ds} after step 2 with experimental v_{ds}.

modeled v_{ds} after step 2 with the experimental v_{ds}. The comparison results show that the modeled v_{ds} waveforms are basically consistent with the experimental results. This is because the switching node voltage is mainly determined by fundamental characteristics of the resonant network, and the impedance fitting result matches impedance of the resonant network well around the switching frequency as shown in Fig. 6 in the main text.

C. Step 3: Solving Differential Equations of the Circuit

Fig. 27 shows the circuit model with ideal power switch. Fig. 28 shows the modeled and experimental v_{ds}. Despite of the deviated waveform, zero-crossing points of v_{ds} are basically the same owing to the use of charge-based equivalent capacitance. This indicates the proposed model can predict the correct switch timing to achieve ZVS.

Furthermore, the optimal duty ratios (D_B) under different switching frequencies are calculated according to zero-crossing

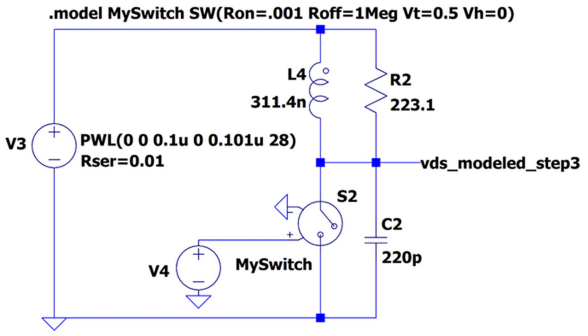

Fig. 27. Circuit model with ideal switch.

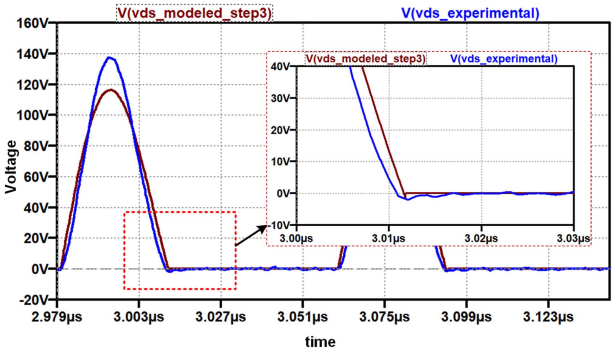

Fig. 28. Comparison of modeled v_{ds} after step 3 with experimental v_{ds}.

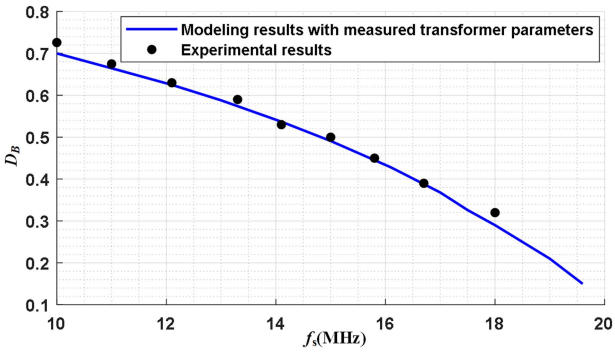

Fig. 29. Comparison of modeled and experimental D_B.

points of v_{ds}. To reduce the modeling errors, parameter changes of the air core transformer are tested with impedance analyzer and considered in the model. The modeled and experimental D_B are shown in Fig. 29, which shows the modeling results match the experimental results well.

Appendix B

This appendix provides the transformer characteristics acquired from impedance analyzer. The air core transformer is tested with impedance analyzer 4294 A from Agilent, and the tested results are shown in Fig. 30. The primary inductance under open secondary coil increases from 423.9 nH to 498.3 nH over the operation range, representing a 16.3% increase. The secondary inductance under open primary coil increases from

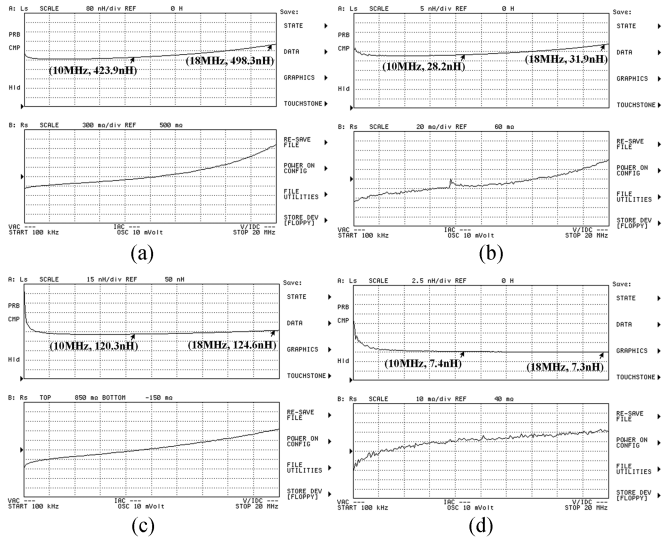

Fig. 30. Transformer characteristics acquired from impedance analyzer. (a) Primary characteristic under open secondary coil. (b) Secondary characteristic under open primary coil. (c) Primary characteristic under shorted secondary coil. (d) Secondary characteristic under shorted primary coil.

28.2 nH to 31.9 nH, representing a 13.1% increase. The primary inductance under shorted secondary coil increases from 120.3 nH to 124.6 nH, representing a 3.6% increase. The secondary inductance under shorted primary coil reduces from 7.4 nH to 7.3 nH, representing a 1.4% reduction. Based on the tested results, the values of L_m and L_k are calculated. The calculated L_m changes from 358.6 nH to 430.8 nH (20.1% increase), and L_k changes from 65.3 nH to 67.5 nH (3.4% increase).

References

[1] X. Hao, J. Zou, K. Yin, X. Ma, and T. Dong, "Enhanced power conversion capability of class-E power amplifiers with GaN HEMT based on cross-quadrant operation," *IEEE Trans. Power Electron.*, vol. 37, no. 11, pp. 13966–13977, Nov. 2022.

[2] G. Zhang, Y. He, S. S. Yu, Y. Zhang, and C. K. Tse, "Switching transition modeling of eGaN HEMT in power converters," *IEEE Trans. Power Electron.*, vol. 38, no. 4, pp. 4251–4256, Apr. 2023.

[3] L. Zeng, Y. Chen, B. Zhang, and D. Qiu, "Accurate modeling of the VHF resonant boost converter considering multiple parasitic parameters," *IEEE Trans. Power Electron.*, vol. 37, no. 12, pp. 14902–14915, Dec. 2022.

[4] Y. Guan, Z. Shi, C. Liu, Y. Wang, and D. Xu, "A 10 MHz DC/DC converter with zero-phase difference synchronous driving signal," *IEEE Trans. Power Electron.*, vol. 36, no. 12, pp. 13878–13888, Dec. 2021.

[5] Y. Guan et al., "Analysis and design of high-frequency converter with resistive matching network and spiral inductor," *IEEE Trans. Power Electron.*, vol. 33, no. 6, pp. 5062–5075, Jun. 2018.

[6] Y. Guan, Y. Wang, W. Wang, and D. Xu, "A high-performance isolated high-frequency converter with optimal switch impedance," *IEEE Trans. Ind. Electron.*, vol. 66, no. 7, pp. 5165–5176, Jul. 2019.

[7] Y. Yanagisawa, Y. Miura, H. Handa, T. Ueda, and T. Ise, "Characteristics of isolated DC–DC converter with class Phi-2 inverter under various load conditions," *IEEE Trans. Power Electron.*, vol. 34, no. 11, pp. 10887–10897, Nov. 2019.

[8] Z. Zhang, K. Xu, Z. W. Xu, J. Xu, X. Ren, and Q. Chen, "GaN VHF converters with integrated Air-Core transformers," *IEEE Trans. Power Electron.*, vol. 34, no. 4, pp. 3504–3515, Apr. 2019.

[9] Z.-L. Zhang, Z. Dong, X.-W. Zou, and X. Ren, "A digital adaptive driving scheme for eGaN HEMTs in VHF converters," *IEEE Trans. Power Electron.*, vol. 32, no. 8, pp. 6197–6205, Aug. 2017.

[10] Z. Zhang, J. Lin, Y. Zhou, and X. Ren, "Analysis and decoupling design of a 30 MHz resonant SEPIC converter," *IEEE Trans. Power Electron.*, vol. 31, no. 6, pp. 4536–4548, Jun. 2016.
[11] Y. Guan, X. Hu, S. Zhang, Y. Wang, D. Xu, and W. Wang, "A novel single switch high-frequency DC/DC converter and its mathematical model," *IEEE Trans. Ind. Appl.*, vol. 55, no. 4, pp. 3877–3888, Jul./Aug. 2019.
[12] Z. Zhang, X. W. Zou, Z. Dong, Y. Zhou, and X. Ren, "A 10-MHz eGaN isolated class-Φ_2 DCX," *IEEE Trans. Power Electron.*, vol. 32, no. 3, pp. 2029–2040, Mar. 2017.
[13] Y. Li, X. Ruan, L. Zhang, J. Dai, and Q. Jin, "Variable switching frequency ON–OFF control for class E DC–DC converter," *IEEE Trans. Power Electron.*, vol. 34, no. 9, pp. 8859–8870, Sep. 2019.
[14] Y. Li, X. Ruan, L. Zhang, and Y. K. Lo, "Multipower-level hysteresis control for the class E DC–DC converters," *IEEE Trans. Power Electron.*, vol. 35, no. 5, pp. 5279–5289, May 2020.
[15] A. Celentano, F. Pareschi, R. Rovatti, and G. Setti, "A Zero-transient dual-frequency control for class-E resonant DC–DC converters," *IEEE Trans. Power Electron.*, vol. 38, no. 2, pp. 2105–2114, Feb. 2023.
[16] H. M. Maheri, D. Vinnikov, A. Chub, V. Sidorov, and I. Galkin, "Application of cycle skipping modulation in Buck–Boost photovoltaic microconverters," *IEEE Trans. Ind. Appl.*, vol. 58, no. 4, pp. 4804–4815, Jul./Aug. 2022.
[17] S. Xu, A. Iwasaki, and H. Sekiya, "Experimental evaluations of thinned-out and PDM controlled class-D rectifier," in *Proc. Int. Conf. Smart Grid*, 2018, pp. 76–81.
[18] A. Shigeno and H. Koizumi, "Half-wave class DE low dv/dt rectifier using thinned-out method with delta-sigma modulation," in *Proc. IEEE Energy Convers. Congr. Expo.*, 2017, pp. 5638–5644.
[19] K. Surakitbovorn and J. M. Rivas-Davila, "Modular ON/OFF and phase-shifting for high-speed radio frequency power modulation," *IEEE Open J. Power Electron.*, vol. 1, pp. 393–406, 2020.
[20] J. Hur et al., "A multilevel class-D CMOS power amplifier for an out-phasing transmitter with a nonisolated power combiner," *IEEE Trans. Circuits Syst. II: Exp. Briefs*, vol. 63, no. 7, pp. 618–622, Jul. 2016.
[21] M. P. Madsen, A. Knott, M. A. E. Andersen, and D. J. Perreault, "Out-phasing control of gallium nitride based very high frequency resonant converters," in *Proc. IEEE 16th Workshop Control Model. Power Electron.*, 2015, pp. 1–7.
[22] H. Wang et al., "Pulse frequency modulated interleaved boost-integrated LC series resonant converter with frequency-free designed transformer," *IEEE Trans. Ind. Electron.*, vol. 70, no. 2, pp. 1609–1621, Feb. 2023.
[23] J. S. Kim, J. O. Yoon, and B. D. Choi, "A high-light-load-efficiency low-ripple-voltage PFM buck converter for IoT applications," *IEEE Trans. Power Electron.*, vol. 37, no. 5, pp. 5763–5772, May 2022.
[24] P. K. Chiu, P. Y. Wang, S. T. Li, C. J. Chen, and Y. T. Chen, "A GaN driver IC with novel highly digitally adaptive dead-time control for synchronous rectifier buck converter," in *Proc. IEEE Energy Convers. Congr. Expo.*, 2020, pp. 3788–3792.
[25] P. Y. Wang, P. K. Chiu, S. T. Li, C. J. Chen, and C. C. Hsu, "A 10 MHz GaN driver IC with bang-bang DeadTime control for synchronous rectifier buck converter," in *Proc. IEEE Energy Convers. Congr. Expo.*, 2020, pp. 3776–3781.
[26] W. J. Zhang, Y. Leng, J. Yu, Y. S. Lu, C. Y. Cheng, and W. T. Ng, "An integrated gate driver for e-mode GaN HEMTs with active clamping for reverse conduction detection," in *Proc. 31st Int. Symp. Power Semicond. Devices ICs*, 2019, pp. 83–86.
[27] T. V. Breussegem and M. Steyaert, "A 82% efficiency 0.5% ripple 16-phase fully integrated capacitive voltage doubler," in *Proc. Symp. VLSI Circuits*, 2009, pp. 198–199.
[28] P. H. Chen, H. C. Cheng, and P. H. Chen, "A fully integrated step-down switched-capacitor DC–DC converter with dual output regulation mechanisms," *IEEE Trans. Circuits Syst. II: Exp. Briefs*, vol. 67, no. 9, pp. 1649–1653, Sep. 2020.

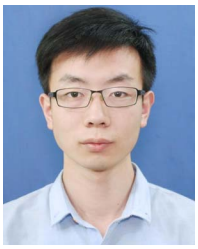

Desheng Zhang received the B.Eng. degree in integrated circuit design & integrated system from the School of Optical and Electronic Information, Huazhong University of Science and Technology, Wuhan, China, in 2018, and the Ph.D. degree in microelectronics & solid-state electronics from the School of Integrated Circuit, Huazhong University of Science and Technology, Wuhan, China, in 2023.

He is currently a Post Doctor researcher with the School of Automation, Wuhan University of Technology, Wuhan, China. His research interests include the design and control of high frequency power converters.

Liangliang Lu received the B.Eng. degree in information engineering and the M.S. degree in aerospace measurement and control technology from Beijing Institute of Technology, Beijing, China, in 2007 and 2010, respectively. He is currently working toward the Ph.D. degree in microelectronics with the School of Optical and Electronic Information, Huazhong University of Science and Technology, Wuhan, China.

From 2010 to 2015, he was the General Designer with the General Design Department, China Academy of Launch Vehicle Technology. Since 2015, he has been the General designer with Lunar Exploration and Space Engineering Center, State Administration of Science, Technology and Industry for National Defense. His current research interests include modeling and control of power converters.

Wei Song received the B.Eng. degree in integrated circuits and systems in 2021 from the School of Optical and Electronic Information, Huazhong University of Science and Technology, Wuhan, China, where he is currently working toward the M.S. degree in integrated circuit engineering with the School of Integrated Circuits.

His current research interests include the control and integration of very high frequency power converter.

Run Min (Member, IEEE) received the B.Eng. degree in microelectronics from the School of Software and Microelectronics, Northwestern Polytechnical University, Xi'an, China, in 2010, and the Ph.D. degree in microelectronics & solid-state electronics from the School of Optical and Electronic Information, Huazhong University of Science and Technology (HUST), Wuhan, China, in 2016.

He is currently an Associate Professor with HUST. His research interests include modelling, analysis, and control of power electronic systems.

Qiaoling Tong (Member, IEEE) received the B.Eng. degree in microelectronics and the Ph.D. degree in microelectronics & solid-state electronics from the School of Optical and Electronic Information, Huazhong University of Science and Technology, Wuhan, China, in 2003 and 2010, respectively.

From 2008 to 2010, he was a Research Scholar with the Department of Electrical Engineering and Computer Science, University of California, Irvine, CA, USA. He is currently a Professor with the School of Integrated Circuits, Huazhong University of Science and Technology, China. His current research interests include sensorless control of dc–dc converters and VLSI implementation of intelligent algorithms.

Qiao Zhang (Member, IEEE) received the B.Eng. degree in automation and the M.Eng. and Ph.D. degrees in control science and control engineering from the Huazhong University of Science and Technology, Wuhan, China, in 2003, 2006, and 2010, respectively.

From 2008 to 2009, he was a Visiting Scholar with the Department of Electronic and Electrical Engineering, University of Sheffield, Sheffield, U.K. From 2009 to 2016, he was a Research Engineer with IMRA Europe U.K. Research Centre. He is currently an Associate Professor with the School of Automation, Wuhan University of Technology, Wuhan, China. His research interests include the power electronics system design and control, such as dc–dc converter sensorless control strategies, electrical machine parameters estimation by control theory, system nonlinearity compensation for dc–dc converters and voltage source inverters.

Han Peng (Senior Member, IEEE) received the B.S. degree from Southeast University, Nanjing, China, and the Ph.D. degree from Rensselaer Polytechnic Institute, Troy, NY, USA, in 2006 and 2011, respectively, both in electrical engineering.

From 2011 to 2017, she was a Lead Electrical Engineer with the Global Research Center of General Electric Company, Niskayuna, NY, USA. Since 2018, she has been a Professor with the Huazhong University of Science and Technology, Wuhan, China. She has authored or coauthored more than 20 papers in refereed journals and international conference proceedings. She has four U.S. patent and two Chinese patents. Her research interests include high frequency, high power density power management IC design, high frequency supply modulators, and applications of wide bandgap power devices. Her research covers various different applications, as energy harvesting, communication power, healthcare electronics, more electrical aircraft systems, and electric vehicles,

Dr. Peng has been an Associate Editor for IEEE TRANSACTIONS ON POWER ELECTRONICS since 2017. She was an Associate Technical Program Chair for 2019 IEEE Energy Conversion Congress and Exposition.

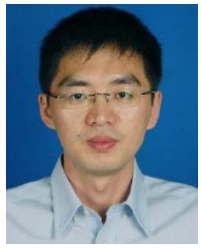

Keliang Zhou (Senior Member, IEEE) received the B.Sc. degree in electrical engineering from the Huazhong University of Science and Technology, Wuhan, China, in 1992, the M.Eng. degree in electrical engineering from the Wuhan University of Technology, Wuhan, China, in 1995, and the Ph.D. degree in electrical engineering from Nanyang Technological University, Singapore, in 2002.

From 2006 to 2019, he was an Academic Staff with Southeast University, Nanjing, China, the University of Canterbury, Christchurch, New Zealand, and the University of Glasgow, Glasgow, U.K., respectively. He is currently a Full Professor and the Head of the School of Automation, Wuhan University of Technology. He has coauthored one monograph and more than 100 peer-reviewed technical articles and holds several granted patents in relevant areas. His main research interests include modeling and control of power converters, advanced control theory and applications, and renewable energy conversion and control.